Fourier-Based Modeling of a Slotless Hybrid Homopolar Radial Magnetic Bearing with Passive Axial Stabilization

1st François Boulanger
Institute of Mechanics, Material and Civil Engineering
Université catholique de Louvain (UCLouvain)
Louvain-la-Neuve, Belgium
francois.boulanger@student.uclouvain.be

2nd Sébastien Bosschaert
Institute of Mechanics, Material and Civil Engineering
Université catholique de Louvain (UCLouvain)
Louvain-la-Neuve, Belgium
sebastien.bosschaert@student.uclouvain.be

3rd Guillaume Colinet
Institute of Mechanics, Material and Civil Engineering
Université catholique de Louvain (UCLouvain)
Louvain-la-Neuve, Belgium
guillaume.colinet@uclouvain.be

4th Bruno Dehez
Institute of Mechanics, Material and Civil Engineering
Université catholique de Louvain (UCLouvain)
Louvain-la-Neuve, Belgium
bruno.dehez@uclouvain.be

2023 IEEE Energy Conversion Congress and Exposition (ECCE) | 979-8-3503-1644-5/23/$31.00 ©2023 IEEE | DOI: 10.1109/ECCE53617.2023.10362844

***Abstract*—Among active magnetic bearings (AMB), homopolar hybrid AMB (HH-AMB) generate a homopolar bias magnetic field using permanent magnets (PM) to reduce Joule and iron losses. The iron losses are further reduced by the slotless topology of the HH-AMB (SHH-AMB). Analytical models of the topology have been implemented using magnetic equivalent circuit (MEC) and Fourier-based (FB) methods. This paper proposes a FB model of a variant of the SHH-AMB topology that has additional saliencies on the rotor to provide an axial stabilization. The validity of the results is assessed with a finite element analysis (FEA) and experimentally, with measurements performed on a prototype of the bearing under study.**

***Index Terms*—Slotless homopolar hybrid active magnetic bearing, Fourier-based model, axial thrust bearing.**

I. INTRODUCTION

Active magnetic bearings (AMB) allow a contactless stabilization of a rotating body through electromagnetic forces. Among the various types of AMB, homopolar hybrid AMB (HH-AMB) generates a homopolar bias magnetic field with permanent magnets (PM) [1]. This topology eliminates Joule losses associated with bias current, thanks to the action of PM. The homopolar nature of the bias magnetic field reduces the iron losses associated with fluctuations in the magnetic field as the rotor spins. These latter losses can be further reduced by placing the armature winding in the airgap, thus avoiding the field discontinuity produced by slot openings.

In [2], this kind of slotless HH-AMB topology (SHH-AMB) is described and studied using magnetic equivalent circuits, with the aim of calculating radial position and current stiffnesses. However, as the developed model roughly approximates the magnetic field distribution, it does not offer a very accurate estimation of these two characteristics. In [3], Fourier-based (FB) analysis is used to accurately determine the magnetic field distribution when the rotor is in the centered position, with the sole assumption that the permeability of ferromagnetic parts is infinite. The predictions on position and current stiffnesses obtained using this model are very close to those predicted by the finite element analysis (FEA), but for low values of radial rotor off-centering.

As the previous work is only considering radial stabilization, the aim of this article is to investigate a SHH-AMB bearing structure that provides passive axial stabilization by introducing axial ferromagnetic saliencies on the rotor. The method used to determine the magnetic field distribution, from which the radial and axial stiffnesses are obtained, is identical to the one used in [4] .

The paper is organized as follows. Section II describes the structure of the SHH-AMB topology as well as its working principle. Section III develops the FB model and the derivation of the stiffnesses, which are then challenged with the FEA in section IV. The experimental validation of the model takes place in section V, in which the prototype and the setup allowing for the measurements are presented.

II. STRUCTURE AND WORKING PRINCIPLE

A. Structure

A schematic 3D view of the SHH-AMB and its rotor saliencies is presented in Fig. 1. The stator is made of two ferromagnetic rings between which a PM ring with axial polarization is inserted. The rotor is made of one hollow piece of ferromagnetic material that has two saliencies, similarly to the stator. The rotor is inserted inside the stator such that the iron saliencies face each other and give rise to an airgap in which two sets of four coils, one set per axis of actuation, are inserted 90° apart. In Fig. 1, the yellow and green sets of windings actuate the x and y-axes of the bearing, respectively.

Authorized licensed use limited to: Univ Catholique de Louvain/UCL. Downloaded on December 09,2024 at 09:56:54 UTC from IEEE Xplore. Restrictions apply.

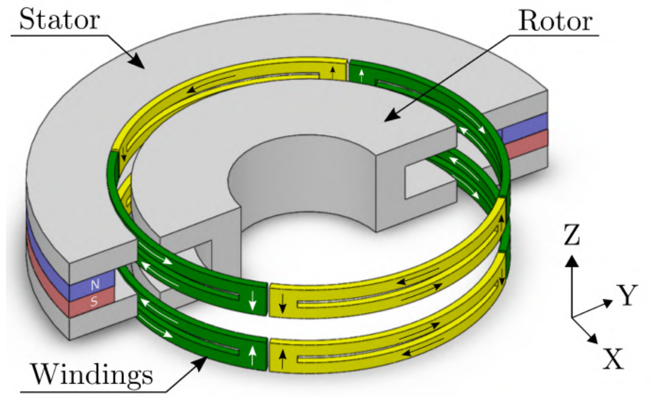

Fig. 1: 3D cross-sectional view of the SHH-AMB with rotor saliencies.

The coils are connected to each other in series and anti-series, so that the current flows in the direction shown in the figure.

Fig. 2 shows a cross-sectional representation of the bearing as well as a detailed definition of each parameter used to describe the dimensions of the bearing. Δ_z represents the axial distance between the stator and rotor symmetry planes. The parameters describing the end windings leave their configuration as general as possible, and in particular inserted and overlapped configurations, as it has been shown in [5] that they improve bearing performances. Each coil of the bearing is made of N_W spires, the PM have a remanent flux density B_{rem} and a relative magnetic permeability $\mu_{r,PM}$.

B. Working Principle

Among the six degrees of freedom of the rotor, five of them must be stabilized by the SHH-AMB: the translations along the x, y and z-axes and the rotation around the x and y-axes. The natural stability of a degree of freedom around its equilibrium point is assessed by introducing a small displacement along the concerned degree of freedom. This latter is stable if the resulting force or torque is opposed to this displacement, and unstable otherwise, in which case an active stabilization is required.

If the rotor is slightly displaced along the z-axis, the alignment of the stator and rotor saliencies is shifted, the magnetic permeance of the airgap is lowered, and the resulting bias magnetic flux is smaller compared to the centered configuration. As the detent forces tend to act to maximize the magnetic flux, the resulting axial force F_z acting on the rotor is upward. The axial z degree of freedom in translation is consequently naturally stable.

The stability of the x and y translations can be assessed by the stability of a radial eccentricity of the rotor because of the revolution symmetry of the bearing. Such a configuration is called radially off-centered, and the eccentricity is noted ϵ. If the rotor shows an eccentricity, the airgap length will be shorter in the direction of the eccentricity and longer in the opposite direction. As a result, the magnetic field density, and therefore the magnetic pressure between rotor and stator, will become unbalanced, creating a net detent force in the direction of eccentricity, making the radial x and y degrees of freedom naturally unstable. Their stabilization is achieved by means of the two windings shown in Fig. 1, the yellow and green ones acting along the x and y-axes respectively. In accordance with the way in which the four coils forming a winding are connected, the injection of a current increases the field density on one side of the concerned winding, while decreasing that on the other, and thus generates, through an imbalance of magnetic pressures, an electrodynamic force whose amplitude and direction depend on those of the current. Controlling them as a function of the radial position of the rotor can therefore counteract the instability caused by the detent forces.

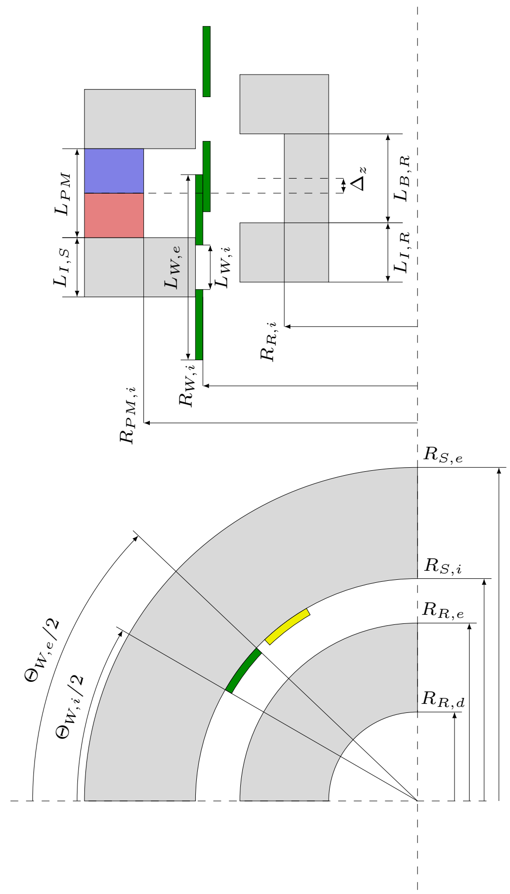

Fig. 2: Cross-sectional views of the SHH-AMB with rotor saliencies and the parameters used to describe its dimensions.

With regard to rotational degrees of freedom around the x and y-axes, they can be simply stabilized by axially duplicating the bearing.

III. Analytical Model

A. Modeling of the Magnetic Forces

Considering small displacements around the equilibrium position $(0, 0, \Delta_{z,0})$, and neglecting the magnetic saturation,

Authorized licensed use limited to: Univ Catholique de Louvain/UCL. Downloaded on December 09,2024 at 09:56:54 UTC from IEEE Xplore. Restrictions apply.

the electromagnetic forces acting on the rotor can be written:

$$\begin{cases} F_x = k_\epsilon \delta_x + k_i i_x & \text{(1a)} \\ F_y = k_\epsilon \delta_y + k_i i_y & \text{(1b)} \\ F_z = F_z|_{\Delta_{z,0}} + k_z \delta_z & \text{(1c)} \end{cases}$$

where δ_x, δ_y and δ_z are the small relative displacements of the rotor along the x, y and z-axes respectively, i_x and i_y are the current flowing through the winding dedicated to the x and y-axes, and k_ϵ, k_i and k_z which are defined as follows:

$$k_\epsilon \triangleq \frac{\partial F_x}{\partial \delta_x} = \frac{\partial F_y}{\partial \delta_y} \quad k_i \triangleq \frac{\partial F_x}{\partial i_x} = \frac{\partial F_y}{\partial i_y} \quad k_z \triangleq \frac{\partial F_z|_{\Delta_{z,0}}}{\partial \delta_z} \tag{2}$$

In this article, these stiffnesses are calculated using the same approach as in [3]. First, the distribution of the magnetic flux density produced by the PM is calculated for a rotor in a centered radial position. This reduces the problem to an axisymmetric 2D case, for which the FB analysis presented in [4] is applicable. The impact of a radial off-centering is then considered through a modulation function based on the local variation of the airgap permeance. The stiffnesses are eventually calculated on this basis, either by integration of the Maxwell Stress Tensor, for the position stiffnesses, or by integration of the flux linked by the windings, for the current stiffness.

B. Magnetic Flux Density Without Radial Eccentricity

To be applied to an axisymmetric problem, the FB approach requires periodicity along the z-axis. This can be obtained artificially by axially repeating the bearing structure. However, the spatial period of this repetition, defined as $2L_{ext}$, must be chosen carefully to limit the impact of one bearing on the other, but also the computational cost for achieving a high spatial resolution of the magnetic fields distribution. On this basis, considering that the problem is static and that the permeability of ferromagnetic parts is infinite, the constitutive equation that the vector potential must satisfy within each of the seven regions shown in Fig. 3, is the following:

$$\frac{1}{r}\frac{\partial}{\partial r}\left(r\frac{\partial A_\theta}{\partial r}\right) + \frac{\partial^2 A_\theta}{\partial z^2} - \frac{A_\theta}{r^2} = 0 \quad \text{in air} \tag{3}$$

$$\frac{1}{r}\frac{\partial}{\partial r}\left(r\frac{\partial A_\theta}{\partial r}\right) + \frac{\partial^2 A_\theta}{\partial z^2} - \frac{A_\theta}{r^2} = -\mu_0 \nabla \times \vec{M} \quad \text{in PM} \tag{4}$$

where $\vec{M}$ is the magnetization of the PM, being only axial in the bearing under study, which gives rise to the following expression:

$$\vec{M} = \frac{B_{rem}}{\mu_0}\hat{z} \tag{5}$$

A local coordinate frame is associated with every region, and the transformation from the main frame to the frame of a region k is: $z_k = z - \Delta_k$.

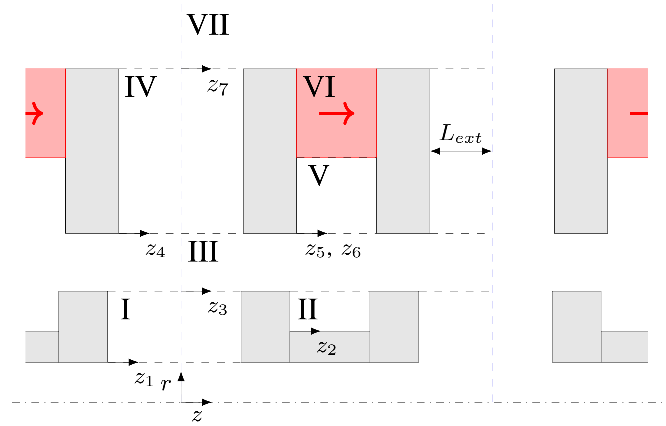

Fig. 3: Subdomain division and periodization of the model.

Solving (3) with the variable separation method gives rise to the following general expression of the radial and axial components of the magnetic flux density in region k:

$$\begin{aligned} B_{k,r}(r, z_k) &= \sum_{p=1}^{n} [B_{r,s}(r)\sin(\omega_k z_k) + B_{r,c}(r)\cos(\omega_k z_k)] \\ B_{k,z}(r, z_k) &= \sum_{p=1}^{n} [B_{z,s}(r)\sin(\omega_k z_k) + B_{z,c}(r)\cos(\omega_k z_k)] \\ &\quad + B_{k,0} \end{aligned} \tag{6}$$

where:

$$B_{r,s}(r) = a_{p,k} I_1(\omega_k r) + b_{p,k} K_1(\omega_k r) \tag{7}$$

$$B_{r,c}(r) = -c_{p,k} I_1(\omega_k r) - d_{p,k} K_1(\omega_k r) \tag{8}$$

$$B_{z,c}(r) = a_{p,k} I_0(\omega_k r) - b_{p,k} K_0(\omega_k r) \tag{9}$$

$$B_{z,s}(r) = c_{p,k} I_0(\omega_k r) - d_{p,k} K_0(\omega_k r) \tag{10}$$

$$\omega_k = \frac{p\pi}{\tau_k} \tag{11}$$

where n is the number of harmonics employed in the model, I_ν and K_ν are the modified Bessel functions of the first and second kinds of order ν, and $a_{p,k}$, $b_{p,k}$, $c_{p,k}$, $d_{p,k}$, $B_{k,0}$ and τ_k are unknown values, determined by the boundary conditions (BC).

The BC can be separated into two categories with respect to their orientation: the radial BC, for boundaries parallel to the r-axis, and the axial BC, for boundaries parallel to the z-axis. The former allow for obtaining the values of the τ_k of the subdomains, while the latter determine the rest of the unknowns.

The first radial BC concerns the periodicity of the solution in subdomains III and VII, which is ensured by the general expression of the magnetic flux density if τ_3 and τ_7 are imposed as half of the axial width of their domain. The second type of radial BC concerns the magnetic conductors that are considered perfect, which implies that the radial magnetic flux density of the regions I, II, IV, V and VI is null at the beginning and at the end of the subdomain. This condition is

Authorized licensed use limited to: Univ Catholique de Louvain/UCL. Downloaded on December 09,2024 at 09:56:54 UTC from IEEE Xplore. Restrictions apply.

ensured by imposing their τ_k as the axial width of the domain and by canceling their $c_{k,p}$ and $d_{k,p}$.

Seven types of axial BC are employed in the model:

1) Neumann BC:

$$B_{II,z}\Big|_{r=R_{R,i}}^{z_2\in[0,\tau_2]}=0 \tag{12}$$

2) Continuous BC:

$$B_{V,r}\Big|_{r=R_{PM,i}}^{z_5\in[0,\tau_5]}=B_{VI,r}\Big|_{r=R_{PM,i}}^{z_6\in[0,\tau_6]} \tag{13}$$

$$H_{V,z}\Big|_{r=R_{PM,i}}^{z_5\in[0,\tau_5]}=H_{VI,z}\Big|_{r=R_{PM,i}}^{z_6\in[0,\tau_6]} \tag{14}$$

3) Combination of Neumann and continuous BC:

$$B_{I,r}\Big|_{r=R_{R,e}}^{z_1\in[0,\tau_1]}=B_{III,r}\Big|_{r=R_{R,e}}^{z_3\in[\Delta_1,\Delta_1+\tau_1]} \tag{15}$$

$$H_{I,z}\Big|_{r=R_{R,e}}^{z_1\in[0,\tau_1]}=H_{III,z}\Big|_{r=R_{R,e}}^{z_3\in[\Delta_1,\Delta_1+\tau_1]} \tag{16}$$

$$B_{II,r}\Big|_{r=R_{R,e}}^{z_2\in[0,\tau_2]}=B_{III,r}\Big|_{r=R_{R,e}}^{z_3\in[\Delta_2,\Delta_2+\tau_2]} \tag{17}$$

$$H_{II,z}\Big|_{r=R_{R,e}}^{z_2\in[0,\tau_2]}=H_{III,z}\Big|_{r=R_{R,e}}^{z_3\in[\Delta_2,\Delta_2+\tau_2]} \tag{18}$$

$$B_{IV,r}\Big|_{r=R_{S,i}}^{z_4\in[0,\tau_4]}=B_{III,r}\Big|_{r=R_{S,i}}^{z_3\in[\Delta_4,\Delta_4+\tau_4]} \tag{19}$$

$$H_{IV,z}\Big|_{r=R_{S,i}}^{z_4\in[0,\tau_4]}=H_{III,z}\Big|_{r=R_{S,i}}^{z_3\in[\Delta_4,\Delta_4+\tau_4]} \tag{20}$$

$$B_{V,r}\Big|_{r=R_{S,i}}^{z_5\in[0,\tau_5]}=B_{III,r}\Big|_{r=R_{S,i}}^{z_3\in[\Delta_5,\Delta_5+\tau_5]} \tag{21}$$

$$H_{V,z}\Big|_{r=R_{S,i}}^{z_5\in[0,\tau_5]}=H_{III,z}\Big|_{r=R_{S,i}}^{z_3\in[\Delta_5,\Delta_5+\tau_5]} \tag{22}$$

$$B_{IV,r}\Big|_{r=R_{S,e}}^{z_4\in[0,\tau_4]}=B_{VII,r}\Big|_{r=R_{S,e}}^{z_7\in[\Delta_4,\Delta_4+\tau_4]} \tag{23}$$

$$H_{IV,z}\Big|_{r=R_{S,e}}^{z_4\in[0,\tau_4]}=H_{VII,z}\Big|_{r=R_{S,e}}^{z_7\in[\Delta_4,\Delta_4+\tau_4]} \tag{24}$$

$$B_{VI,r}\Big|_{r=R_{S,e}}^{z_6\in[0,\tau_6]}=B_{VII,r}\Big|_{r=R_{S,e}}^{z_7\in[\Delta_6,\Delta_6+\tau_6]} \tag{25}$$

$$H_{VI,z}\Big|_{r=R_{S,e}}^{z_6\in[0,\tau_6]}=H_{VII,z}\Big|_{r=R_{S,e}}^{z_7\in[\Delta_6,\Delta_6+\tau_6]} \tag{26}$$

$$H_{III,z}\Big|_{r=R_{R,e}}^{z_3\in[\Delta_1+\tau_1,\Delta_2]\cup[\Delta_2+\tau_2,2\tau_3-\Delta_1]}=0 \tag{27}$$

$$H_{III,z}\Big|_{r=R_{S,i}}^{z_3\in[\Delta_4+\tau_4,\Delta_5]\cup[\Delta_5+\tau_5,2\tau_3-\Delta_5]}=0 \tag{28}$$

$$H_{VII,z}\Big|_{r=R_{S,e}}^{z_7\in[\Delta_4+\tau_4,\Delta_6]\cup[\Delta_6+\tau_6,2\tau_3-\Delta_5]}=0 \tag{29}$$

4) Dirichlet BC:

$$B_{I,r}\Big|_{r=R_{R,d}}^{z_1\in[0,\tau_1]}=0 \tag{30}$$

5) Magnetic flux density at infinite radius:

$$\lim_{r\to\infty} B_{VII,r}=0 \tag{31}$$

$$\lim_{r\to\infty} B_{VII,z}=0 \tag{32}$$

6) Ampere law:

$$B_{I,0}\tau_1=2B_{III,0}\tau_3 \tag{33}$$

$$B_{IV,0}\tau_4+B_{V,0}\tau_5=2B_{III,0}\tau_3 \tag{34}$$

$$1/\mu_{r,PM}(B_{rem}-B_{VI,0})\tau_6=B_{IV,0}\tau_4 \tag{35}$$

7) Magnetic flux conservation:

$$\phi_{III}+\phi_{IV}+\phi_V+\phi_{VI}+\phi_{VII}=0 \tag{36}$$

where ϕ_k is the magnetic flux entering the left stator saliency from region k.

Equations (12) to (36) give rise to a linear system that is inverted numerically, to obtain coefficients $a_{p,k}$, $b_{p,k}$, $c_{p,k}$, $d_{p,k}$ and the DC terms. The general form of the equations forming this system originates from the evaluation of the magnetic flux density for a given radius and is the following:

$$AI_\nu(\omega_k R)+BK_\nu(\omega_k R)=C \tag{37}$$

The ascending and descending natures of the I_ν and K_ν functions, respectively, induce a degradation of the conditioning of the system with increasing number of harmonics n, preventing any improvement in model accuracy. This problem is mitigated by applying a scaling on the modified Bessel functions to give rise to the following new general form of the equations constituting the system:

$$A'\frac{I_\nu(\omega_k R)}{I_0(\omega_k R_{k,0})}+B'\frac{K_\nu(\omega_k R)}{K_0(\omega_k R_{k,0})}=C \tag{38}$$

where $R_{k,0}$ is a scaling radius, chosen as the average of the inner and outer radii of the concerned region.

The number of harmonics employed in a specific region k, n_k, is chosen to ensure a coherent accuracy in every subdomain of the model. A concept of spatial rate of harmonic is introduced to perform a relevant choice, which is defined as: $\eta_k=n_k/\tau_k$. Employing the same value of η_k in every subdomain avoids wasting high-order harmonics. The number of harmonics is thus chosen in one subdomain, arbitrarily region II, and the number of harmonics in the other subdomains is imposed by a law of proportionality over τ_k.

C. Magnetic Flux Density With Radial Eccentricity

In a view of evaluating the radial detent force and the electrodynamic force, it is necessary to take the radial eccentricity of the rotor into account. Two different approaches, allowing for modeling the effect of the radial eccentricity of the rotor, are compared in [3]. The method based on a superposition principle consists in subdividing the machine into several sections along the circumferential direction and solving each of them on the basis of the model without eccentricity, but with a different equivalent airgap. This method proved to be much slower and less accurate than multiplying the solution of the eccentricity-free model by a modulation function (MF), that accounts for the variation of the magnetic permeance of

Authorized licensed use limited to: Univ Catholique de Louvain/UCL. Downloaded on December 09,2024 at 09:56:54 UTC from IEEE Xplore. Restrictions apply.

the airgap. The definition and expression of the MF are the following:

$$\Gamma(\theta,\epsilon) \triangleq \frac{B_{III,r}\Big|_{\epsilon\neq 0}}{B_{III,r}\Big|_{\epsilon=0}} \tag{39}$$

$$= 1 + \frac{\epsilon\cos(\theta)}{R_{S,i}\ln\left(\frac{R_{S,i}}{R_{R,e}}\right)} + \frac{\epsilon^2\cos(2\theta)}{R_{S,i}^2\ln\left(\frac{R_{S,i}}{R_{R,e}}\right)} \tag{40}$$

with $\epsilon = \sqrt{\delta_x^2+\delta_y^2}$ and θ the angular position in the airgap relative to the eccentricity direction.

D. Stiffnesses

The stiffnesses of the bearing are obtained by integration of the magnetic flux densities evaluated above. These forces have two physical origins: the radial and axial stiffnesses originate from detent forces, and the current stiffness from electrodynamic forces.

1) Detent forces: The detent forces are evaluated through the surface integration of the Maxwell Stress Tensor that takes the following expression in this application:

$$\sigma_{MST} = \frac{1}{\mu_0}\begin{pmatrix} \frac{1}{2}B_r^2 & 0 & B_rB_z \\ 0 & 0 & 0 \\ B_rB_z & 0 & \frac{1}{2}B_z^2 \end{pmatrix} \tag{41}$$

The integration surface is an open cylinder situated at the average radius of region III.

The axial force F_z is directly obtained by the integration of the magnetic flux density of the centered configuration, provided by the FB model:

$$F_z = \frac{2\pi R_{MST}}{\mu_0}\int_0^{2\tau_3}\left(B_{III,r}B_{III,z}\right)\Big|_{r=R_{MST}} dz \tag{42}$$

with $R_{MST} = (R_{S,i}+R_{R,e})/2$.

The radial detent force along the x-axis is obtained by integration of the magnetic flux density distribution of the off-centered configuration, obtained with the MF:

$$F_x = \int_0^{2\pi}\int_0^{2\tau_3}\frac{\Gamma(\theta,\delta_x)^2}{2\mu_0}B_{III,r}^2\Big|_{r=R_{MST}} dzd\theta \tag{43}$$

The axial and radial position stiffnesses are eventually obtained by derivation of these forces, in accordance with (2). The derivation of the axial position stiffness is performed numerically, and the radial position stiffness is derived analytically by derivation of (39).

2) Electrodynamic forces: Due to the nature of the electrodynamic force responsible for the current stiffness, the latter can be obtained directly via:

$$k_i = \frac{\partial\Phi_x}{\partial\delta_x} \tag{44}$$

where Φ_x is the magnetic flux circled by the winding of one axis of actuation. This flux is obtained by integrating the magnetic flux density of the off-centered configuration over the four coils constituting a phase:

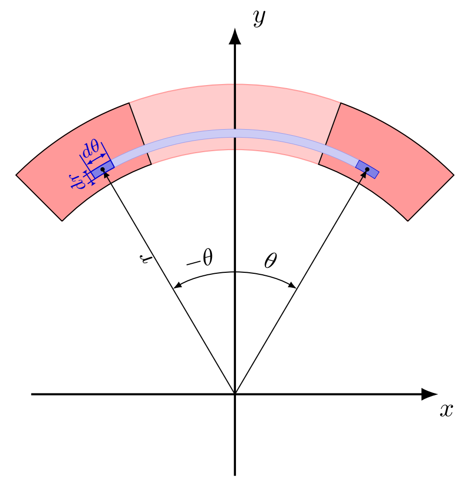

Fig. 4: Cross-section of the infinitesimal elementary winding.

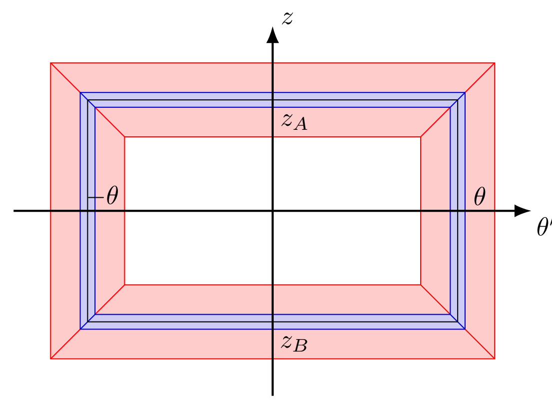

Fig. 5: Representation of the elementary winding path in the $r-\theta$ plane.

$$\Phi = \sum_{j=1}^{4}\Phi_j = \sum_{j=1}^{4}\int_{R_{W,i}}^{R_{S,i}}\int_{\Theta_{W,i,j}}^{\Theta_{W,e,j}} d\Phi_j \tag{45}$$

where $d\Phi_j$ is the magnetic flux through an elementary winding of infinitesimal cross-section $dS = rdrd\theta$, illustrated in Fig. 4, whose outwards and inwards conductors are located in (r,θ) and in $(r,-\theta)$, respectively. The expression of the magnetic flux $d\Phi_j$ is the following:

$$d\Phi_j = \frac{N_W}{S_W}dS\int_{-\theta}^{\theta}\int_{z_A(\theta)}^{z_B(\theta)} B_{III,r}(r,z)\Gamma(\theta',\epsilon)rd\theta' dr \tag{46}$$

where z_A and z_B are respectively the axial beginning and end of the winding, and are functions of θ (Fig. 5). As for the radial position stiffness, the current stiffness is obtained by analytical derivation of the MF with respect to ϵ.

IV. Finite Element Validation

The results provided by the model are first validated through a FEA. Two bearings are considered for this purpose, and

Authorized licensed use limited to: Univ Catholique de Louvain/UCL. Downloaded on December 09,2024 at 09:56:54 UTC from IEEE Xplore. Restrictions apply.

TABLE I: Parameters of the bearings

Parameter	***Bearing*** I	***Bearing*** II	***Unit***
$L_{I,S}$	5	10	mm
L_{PM}	21	15	mm
$L_{I,R}$	10	10	mm
$L_{B,R}$	22	15	mm
$L_{W,i}$	8	8	mm
$L_{W,e}$	44	15	mm
$R_{R,d}$	24.5	45	mm
$R_{R,i}$	36	60	mm
$R_{R,e}$	111	72	mm
$R_{S,i}$	121	75	mm
$R_{PM,i}$	121	85	mm
$R_{S,e}$	130	105	mm
$R_{W,i}$	119	74	mm
$\Theta_{W,i}$	72	75	$\circ$
$\Theta_{W,i}$	89	89	$\circ$
$\Delta_{z,0}$	-6	-1	mm
B_{rem}	1.008	1.44	T
$\mu_{r,PM}$	1.05	1.05	/
N_W	41	10	/

their respective dimensions and configurations are listed in Table I. The results are validated at both a local level, with the magnetic flux density distribution, and at a global level, with the stiffnesses.

A. Local Distribution of the Magnetic Flux Density

Fig. 6 shows the radial and axial components of the magnetic flux density in the middle of the airgap of the bearing I as a function of z, for a radially centered rotor. The results obtained with the FB model for different numbers of harmonics are compared to the results provided by the 2D FEA. The solution converges towards the results obtained with the FEA as the number of harmonics is increased, which validates the FB model. The amplitude of the radial magnetic flux density tends to be overestimated by the FB model for lower numbers of harmonics.

The validity of the MF is assessed by comparing the magnetic flux density distribution obtained with the FB model and the MF and by a 3D FEA. The radial eccentricity of the rotor is set at 2 $\%$ of the airgap, i.e., 500 μm. The results of this analysis are presented in Fig. 7. In the airgap, i.e. for axial positions such that the ferromagnetic stator rings and the ferromagnetic rotor saliencies face each other, the MF tends to produce an accurate approximation of the effect of the eccentricity. However, this effect is overestimated outside the airgap.

B. Stiffnesses

Table II shows the values of the three stiffnesses obtained with the FB model with different numbers of harmonics and the results provided by 3D FEA. The axial stiffness tends to converge toward the results of the FEA as the number of harmonics increases. If the number of harmonics is low, the value is overestimated, similarly to the amplitude of the radial magnetic flux density. Regarding the radial and current stiffnesses, although their values tend to get closer to the results of the FEA as the number of harmonics increases, significant errors remain. These errors originate from the invalidity of the MF outside the airgap. As the machine I presents a large airgap and disproportionate rotor and stator saliencies, the whole machine tends to contribute to k_i and k_ϵ, even where the MF is not accurate. The machine II of Table I presents a shorter airgap length, and stator and rotor saliencies of the same axial length. The stiffnesses of such a machine are shown in Table III, where it can be observed that k_i and k_ϵ are approached more accurately by the FB model and its MF.

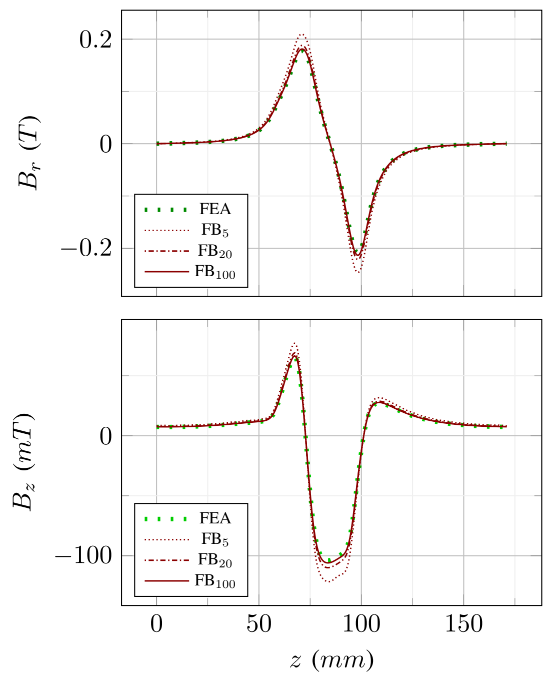

Fig. 6: Airgap radial (B_r) and axial (B_z) magnetic flux density distributions in bearing I, obtained in region II with the FEA and the Fourier-Based model, with different numbers of harmonics (FB_{n_2}).

TABLE II: Stiffnesses of bearing I

Model	***FB***$_5$	***FB***$_{20}$	***FB***$_{100}$	FEA	Error (%)
k_z (N/mm)	10.52	8.535	7.92	7.313	8.30
$k_\epsilon (N/mm)$	34.75	28.101	26.05	18.51	40.73
$k_i (N/A)$	9.58	8.61	8.29	3.625	128.6

V. Experimental Validation

In order to validate the results obtained theoretically, a prototype corresponding to the dimensions of bearing I was

TABLE III: Stiffnesses of bearing II

Model	***FB***$_5$	***FB***$_{20}$	***FB***$_{100}$	***FEA***	Error (%)
k_z (N/mm)	232.95	215.21	210.50	205.38	2.49
$k_\epsilon (N/\mu m)$	1.28	1.21	1.18	1.14	3.51
$k_i (N/A)$	15.77	15.19	14.95	13.13	13.86

Authorized licensed use limited to: Univ Catholique de Louvain/UCL. Downloaded on December 09,2024 at 09:56:54 UTC from IEEE Xplore. Restrictions apply.

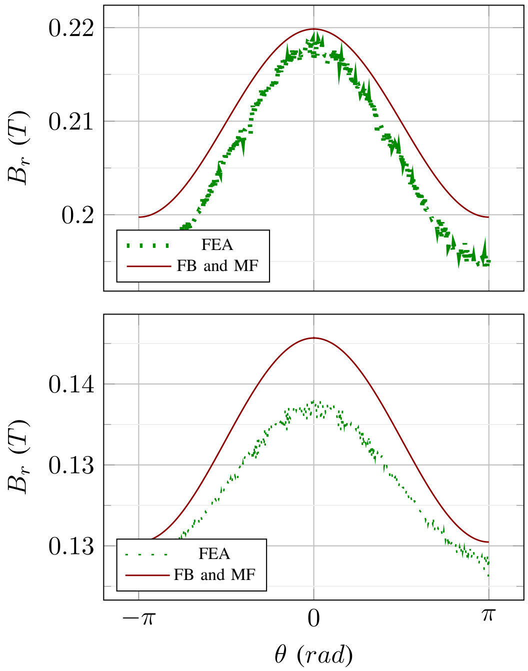

Fig. 7: Airgap radial magnetic flux density distribution (B_r) in bearing I inside (up) and outside (down) the airgap for a rotor off-centered by 200 μm. Comparison between FEA and modulation function.

TABLE IV: Experimental validation of the model

	Exp.	$\boldsymbol{FB}_{100}$	Error (%)	***FEA***	Error (%)
k_z (N/mm)	7.47	7.924	6.07	7.313	2.14
k_ϵ (N/mm)	21.44	26.05	21.5	18.51	13.4
k_i (N/A)	3.863	8.29	114.7	3.625	5.72

built and experimentally characterized. This prototype, and the experimental setup used to measure position and current stiffnesses, are illustrated in Fig. 8. This setup is based on a 5-axis CNC milling machine and a 6-axis force sensor, model F/T 65/5 from ATI. The sensor measures the three force components acting on the rotor, which is positioned relative to the stator by the CNC machine. The results are shown in Table IV, together with those obtained using the FB model. Overall, they confirm the observations made on the basis of the FEA, namely that the proposed model satisfactorily predicts the axial position stiffness, but fails to predict the radial position and the current stiffnesses, demonstrating the limitations of the MF used to predict the effect of eccentricity.

VI. Conclusion

In this paper, an analytical model of a slotless homopolar hybrid active radial magnetic bearing, with passive axial suspension, has been developed to characterize the position and current stiffnesses of such a bearing. This model uses the Fourier method to determine the magnetic flux density distribution when the bearing is radially centered, and a modulation function based on the local variation in airgap permeance to take into account the impact of off-centering on this field distribution. On this basis, the radial and axial position stiffnesses are calculated by integrating the Maxwell Stress Tensor, and the current stiffness is obtained by integrating the flux linked by the windings. The validity of this model is finally assessed by means of 2D and 3D finite element simulations, as well as by the experimental characterization of a prototype. This validation shows that the proposed model is able to correctly predict the axial stiffness for any bearing size, but that the radial and current stiffnesses are poorly estimated for airgaps whose radial thickness to axial length ratio is high. This observation confirms that the Fourier model developed for the centered position is valid, but that the modulation function needs to be revised to take better account of the effect of off-centering out of the bearing airgap.

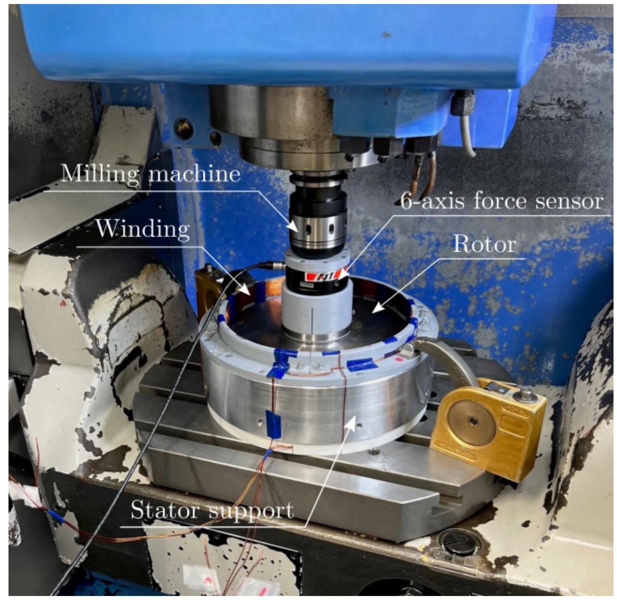

Fig. 8: Experimental setup.

References

[1] F. Jiancheng, W. Xi, W. Tong, T. Enqiong, and F. Yahong, "Homopolar 2-pole radial permanent-magnet biased magnetic bearing with low rotating loss," *IEEE Transactions on Magnetics*, vol. 48, no. 8, pp. 2293–2303, 2012.

[2] G. Colinet and B. Dehez, "Investigations of a new slotless homopolar hybrid active magnetic bearing," 2021. [Online]. Available: 10.1109/TIE.2011.2161056

[3] ——, "Modeling of magnetic field distribution in slotless homopolar active magnetic bearing with eccentricity using fourier analysis," in *2022 25th International Conference on Electrical Machines and Systems (ICEMS)*, 2022, pp. 1–6.

[4] B. L. J. Gysen, K. J. Meessen, J. J. H. Paulides, and E. A. Lomonova, "General formulation of the electromagnetic field distribution in machines and devices using fourier analysis," *IEEE Transactions on Magnetics*, vol. 46, no. 1, pp. 39–52, 2010.

[5] G. Colinet and B. Dehez, "Influence of end winding configuration on the performance of slotless homopolar hybrid active magnetic bearings," in *2021 24th International Conference on Electrical Machines and Systems (ICEMS)*. Gyeongju, Korea, Republic of: IEEE, Oct 2021, p. 530–535. [Online]. Available: https://ieeexplore.ieee.org/document/9634351/

Authorized licensed use limited to: Univ Catholique de Louvain/UCL. Downloaded on December 09,2024 at 09:56:54 UTC from IEEE Xplore. Restrictions apply.